


PAPER

[View Article Online](#)
[View Journal](#) | [View Issue](#)
Cite this: *Nanoscale*, 2020, **12**, 10656

Uniform Pt nanoparticles supported on urchin-like mesoporous TiO₂ hollow spheres as stable electrocatalysts for the oxygen reduction reaction†

 Suqiong He,^{a,b} Chuxin Wu,^b Zhen Sun,^{a,b} Yang Liu,^b Rongtao Hu,^b Lunhui Guan *^b and Hongbing Zhan*^a

In order to promote the commercial application of proton exchange membrane fuel cells, it is of great importance to develop Pt-based electrocatalysts with high activity and stability for the oxygen reduction reaction (ORR). Here, urchin-like mesoporous TiO₂ hollow spheres (UMTHS) with a high specific surface area (167.1 m² g⁻¹) and improved conductivity were designed and applied as supports to disperse Pt nanoparticles (NPs) for the first time. Uniform Pt NPs (~3.2 nm) on the surface of nanothorns were obtained after heat treatment. The as-prepared product (Pt/UMTHS) exhibited a more positive half-wave potential (*E*_h) than that of the reference sample Pt/C without UMTHS (0.867 V vs. 0.829 V). The improved performance can be ascribed to the high specific surface area of UMTHS. The Pt/UMTHS also exhibited a much better ORR stability than the commercial Pt/C after long-term cycling at 0.6–1.0 V according to the comparison of *E*_h, mass activity and electrochemical surface area with Pt/C. The enhanced stability of Pt/UMTHS was mainly derived from the strong metal support interaction between Pt NPs and UMTHS, together with the spatial restriction and the anti-restriction provided by UMTHS.

Received 27th December 2019,

Accepted 15th April 2020

DOI: 10.1039/c9nr10890d

rsc.li/nanoscale

1. Introduction

Proton exchange membrane fuel cells (PEMFCs) have been applied in the automotive industry as energy conversion devices in recent years because of their high energy density, high energy conversion efficiency and low pollution of the environment.^{1–3} However, the cathodic reaction, the oxygen reduction reaction (ORR), needs Pt as the catalyst to accelerate its sluggish kinetics, which seriously hinders the commercial application of PEMFCs owing to their high cost deriving from Pt. Up to now, carbon black supported platinum nanoparticles (Pt/C) have been successfully applied as cathodic catalysts in commercial PEMFCs.^{4–6} However, the usage of Pt/C usually results in the following problems in PEMFCs: (1) the dissolution of Pt followed by the grain growth due to Ostwald ripening, (2) migration and coalescence of Pt NPs due to weak interaction between Pt NPs and carbon supports,

(3) detachment and/or aggregation of Pt NPs which derives from the fatal electrochemical carbon corrosion occurring under repeated start-stop cycles.^{7–9} These will result in the attenuation of ORR activity and lifetime of PEMFCs, producing more difficulties in realizing the final lifetime goals of 8000 h for cars and 20 000 h for buses (target set by the U.S. DOE).¹⁰ Therefore, developing novel supports with a high specific surface area (SSA) whose merits can comprise strong anti-dissolution to acid media and/or anti-corrosion at high potential, and strong interaction with Pt NPs is an effective solution for the efficient dispersion and improved stability of Pt NPs.

Fortunately, TiO₂, one of the promising alternative supports because of its low cost, environmental friendliness, good stability in acid media, anti-corrosion at high potential and strong metal support interaction (SMSI), has drawn much attention over the last decade.^{11–15} Furthermore, it has been demonstrated that the SMSI can enhance the stability of Pt NPs *via* reducing the vacancy of the d band of Pt.^{11,16–19} TiO₂ is a semiconductor, thus it is necessary to improve its conductivity. Thanks to the many efforts devoted by the researchers, the conductivity of TiO₂ has been improved dramatically through doping with a transition metal (Mo/V/Nb) or forming a composite with a carbon material.^{19–23} However, compared with the SSA of carbon black, such as Vulcan XC72 (232 m² g⁻¹),²⁴ the commercial TiO₂ (Degussa P25) exhibits a much lower SSA

^aCollege of Materials Science and Engineering, Fuzhou University, Fuzhou 350108, Fujian, China. E-mail: hbzhan@fzu.edu.cn

^bCAS Key Laboratory of Design and Assembly of Functional Nanostructures, Fujian Key Laboratory of Nanomaterials, Fujian Institute of Research on the Structure of Matter, Chinese Academy of Sciences, Fuzhou 350116, Fujian, China.

E-mail: guanlh@fjirsm.ac.cn

†Electronic supplementary information (ESI) available. See DOI: 10.1039/c9nr10890d

($50 \text{ m}^2 \text{ g}^{-1}$) due to its insufficient pore structure and spherical morphology.²⁵ It is well known that SSA is another important factor needed to be considered when evaluating the properties of the support, because low SSA will impede the uniform dispersion of Pt NPs.^{26–29} Herein, urchin-like mesoporous TiO_2 spheres (UMTHS) with a high SSA ($167.1 \text{ m}^2 \text{ g}^{-1}$) were prepared and used as supports. Then, a Pt-aniline complex was used as both the Pt source and carbon source to improve the conductivity of UMTHS by forming a UMTHS/carbon composite. Uniform Pt NPs ($\sim 3.2 \text{ nm}$) on the surface of nanothorns were obtained. The as-prepared product (denoted as Pt/UMTHS) exhibited a more positive half-wave potential (E_h) than that of the reference sample without UMTHS. More importantly, Pt/UMTHS exhibited a much better ORR stability than the commercial Pt/C after 10 000 cycles at 0.6–1.0 V. The enhanced stability of Pt/UMTHS was mainly ascribed to the SMSI between Pt NPs and UMTHS. Moreover, UMTHS with an urchin-like structure and high SSA also contribute to the enhanced stability of Pt/UMTHS *via* spatial restriction.

2. Experimental

2.1 Materials preparation

UMTHS were synthesized *via* a two-step approach with some modification.³⁰ At first, $420 \mu\text{L}$ $\text{NH}_3\cdot\text{H}_2\text{O}$ (28 wt%) and $910 \mu\text{L}$ H_2O were added successively into a mixed solution consisting of 150 mL anhydrous ethanol and 100 mL acetonitrile under vigorous stirring. Then, 5 mL titanium isopropoxide (TTIP) was promptly injected into the above solution. After stirring for 6 h, the white precipitate, namely amorphous hydrate TiO_2 spheres (AHTSS), was obtained by centrifugation. Finally, AHTSS were dried at 80°C in an air oven overnight after being washed with ethanol and deionized water thrice, respectively. To prepare UMTHS, 1.3 g AHTSS was dispersed in 26 mL H_2O for 30 min ultrasonication. Then, 156 mg NH_4F was added. After stirring for 1 h, 130 mg polyvinyl pyrrolidone (PVP $M_w = 10\,000$) was added to the above solution and stirred for another 1 h. Next, the uniform mixed solution was transferred to a 50 mL Teflon-lined autoclave and set at 110°C for 4 h. After filtration, washing and drying under the same conditions mentioned above, UMTHS were obtained by calcinating the white powders at 350°C for 2 h at a heat rate of 1° min^{-1} under nitrogen protection.

$\text{H}_2\text{PtCl}_6\cdot 6\text{H}_2\text{O}$ and aniline were selected to prepare the Pt-aniline complex with some modifications.³¹ To obtain Pt/UMTHS, 20 mg UMTHS and 14.5 mg Pt-aniline complex were dissolved in 40 mL anhydrous ethanol by 30 min sonication. The homogeneous purple suspension was evaporated and dried in an air oven at 60°C . The obtained dark purple powders were heated to 600°C (5°C min^{-1}) in a furnace tube under the flow of nitrogen and kept for 1 h. For comparison, Pt-aniline was heated under the same conditions without the addition of UMTHS and the black powders obtained were referred to as the Pt@C (w/o UMTHS) sample.

2.2 Physical and chemical characterization

The structures of the obtained products were characterized through powder X-ray diffraction (XRD, Miniflex600). The morphology structure of all the samples was investigated by field emission scanning electron microscopy (FE-SEM, SU8010). Transmission electron microscopy (TEM) and high-resolution TEM (HR-TEM) images were obtained by using a Talos-F200X (FEI). The size distribution was analyzed using Image J. software. The specific surface area of AHTSS and UMTHS was measured by using a Brunauer–Emmett–Teller surface area analyzer (BET, Autosorb IQ). Surface properties were characterized by using an X-ray photoelectron spectrometer (XPS, ESCALAB 250Xi). The Pt content of the Pt/UMTHS and Pt@C (w/o UMTHS) sample was examined by using an inductively coupled plasma optical emission spectrometer (ICP-OES, Ultima-2).

2.3 Electrochemical analysis

A conventional three-electrode system from the CHI760E electrochemical workstation (Shanghai Chenhua Instrument Corporation, China) was used to measure the ORR performance of the as-synthesized samples. A glassy carbon rotating disk electrode (RDE, 0.196 cm^2), Pt foil and Ag/AgCl (saturated, 0.197 V vs. NHE) electrode were used as the working electrode, counter electrode and reference electrode, respectively. 5 mg mL^{-1} catalyst ink was prepared by mixing 2 mg synthetic catalyst and 1 mg acetylene carbon black (to further improve the conductivity of Pt/UMTHS) in a solution containing $590 \mu\text{L}$ iso-propanol and $12 \mu\text{L}$ Nafion (5 wt%) and sonicating the mixture for 30 min. A suitable amount of ink was dropped onto the GC surface several times to make the Pt loading reach $76.5 \mu\text{g}_{\text{Pt}} \text{ cm}^{-2}$. After drying in air without any heat treatment, a uniform catalyst film was obtained. The commercial Pt/C (20 wt%, Johnson-Matthey) and reference sample without the UMTHS (denoted as Pt@C (w/o UMTHS)) sample were used for comparison with the same Pt loading. Cyclic voltammetry (CV) was performed at 0.05–1.05 V (vs. RHE) in O_2 -saturated 0.1 M HClO_4 (100 mV s^{-1}) to activate catalysts. To assess the ORR activity of the as-prepared samples, a linear sweep voltammetry (LSV) curve was obtained in 0.1 M HClO_4 (O_2 , 10 mV s^{-1} , 0.05–1.05 V vs. RHE, 25°C , anodic sweep). The ECSA was evaluated *via* the H_{UPD} method. The hydrogen absorption region of the CV curve tested in 0.1 M HClO_4 (N_2 , 100 mV s^{-1}) was selected for ECSA calculation. The calculation formula for ECSA is: $\text{ECSA} = Q_{\text{H}} / (210 \mu\text{C cm}_{\text{Pt}}^{-2} m_{\text{Pt}}^{-1})$.³² The accelerated durability test (ADT) was conducted at 0.6–1.0 V (vs. RHE, 25°C , 100 mV s^{-1}) up to 10k cycles. For comparison, CV and LSV curves were collected after every 5k and 10k potential cycles. When the ADT test was finished, the used catalysts on the GC surface were collected by sonication in ethanol and centrifugation, and then these samples were sent to be characterized by HR-TEM. The electron transfer number (n) of Pt/UMTHS was obtained through the Koutecky–Levich equation.³³

3. Results and discussion

3.1 Structure and morphology characterization of UMTS and AHTSS

XRD provided direct information on the structure evolution of the samples. The structure of TiO_2 changed from amorphous to anatase after the hydrothermal reaction. As shown in Fig. 1a, all the diffraction peaks found in the UMTS sample were consistent with those of anatase TiO_2 (PDF No. 21-1272), however, an extremely wide and short diffraction peak appeared barely in the two theta range between nearly 16° and 38° in AHTSS, illustrating that the structure of AHTSS was

amorphous (Fig. S1†). XPS was used to investigate the surface composition of the as-prepared samples. As shown in Fig. S2a,† the survey spectrum of XPS suggested that UMTS were composed of only Ti and O elements.

A significant surface morphology change from AHTSS to UMTS can be found through the SEM analysis. As shown in Fig. 2a and b, an urchin-like sphere morphology with a hierarchical structure, which consists of a large number of radially standing 1D nanothorns, appears in the UMTS sample. The mean size of UMTS is around 713 nm (Fig. 2c), obtained by counting 100 randomly distributed NPs (Fig. S3†). Moreover, as identified by TEM observation (Fig. 1d), the interior struc-

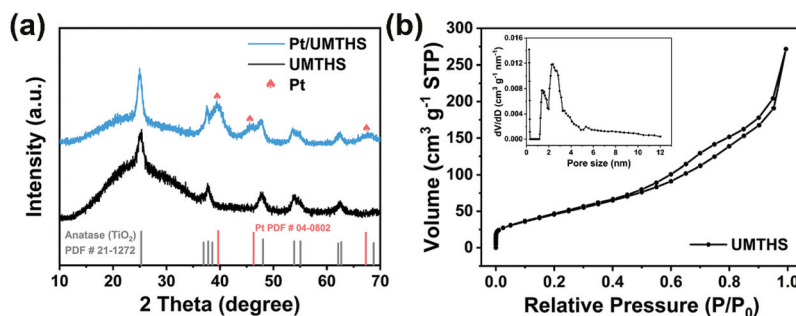


Fig. 1 (a) XRD pattern obtained for UMTS and Pt/UMTS (scan rate: 1° min^{-1}). (b) Nitrogen sorption isotherm and pore size distribution (inset) of UMTS.

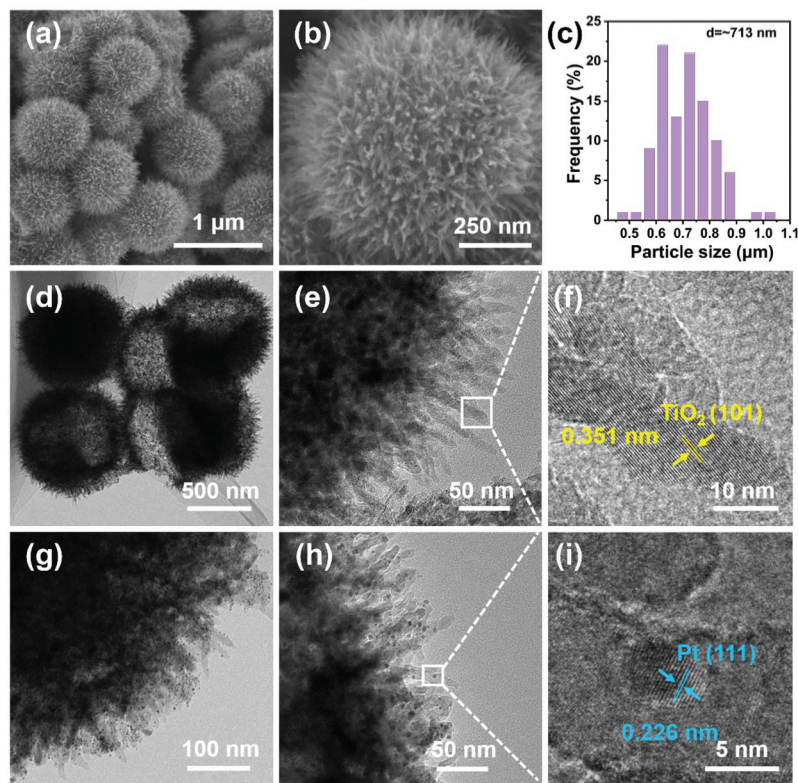


Fig. 2 (a) and (b) Different magnification SEM images of UMTS. (c) Size distribution of UMTS. TEM (d and e) and HR-TEM (f) images of UMTS. TEM (g and h) and HR-TEM (i) images of Pt/UMTS.

ture of UMTHS is hollow which can be further revealed by some broken spheres shown in Fig. S4a and S4b.† Besides, the interior diameter of the hollow sphere is around 645 nm (Fig. S5†). Through HR-TEM characterization (Fig. 2e), it is found that each nanothorn has a rough and irregular surface with a length ranging from 63 to 70 nm. By magnifying the solid square area inserted in Fig. 2e, regular lattice fringes ($d = 0.351$ nm), belonging to the (101) plane of anatase, can be observed clearly in Fig. 2f, which coincides with the XRD result presented above. However, the surface morphology of AHTSS is a big solid sphere with a mean size of around 650 nm (Fig. S2a–S2d†). The sphere-like morphology can also be seen in the TEM results of AHTSS (Fig. S6a–S6b†), elucidating that the morphology of TiO_2 will change from sphere to urchin-like sphere after the hydrothermal reaction. Sphere-like AHTSS was firstly etched by F^- under the physical separation of PVP, and the TiO_2 , originating from the dissolved Ti^{4+} cation, re-deposited radially on the surface of the sphere and then crystallized, resulting in the change from sphere-like AHTSS to urchin-like UMTHS after the hydrothermal reaction.³⁰ Moreover, it can be observed clearly that there are plenty of small spheres and pores in the magnified area of AHTSS, suggesting that AHTSS is stacked by these small spheres.

In addition, AHTSS and UMTHS were studied through nitrogen adsorption–desorption isotherms to check their SSA and pore structure. AHTSS exhibited a type-I isotherm plot (Fig. S7a†), while UMTHS performed a type-IV isotherm plot with a H3 hysteresis loop (Fig. 1b). The SSA of AHTSS was $421.3 \text{ m}^2 \text{ g}^{-1}$ and the pore size distribution result of AHTSS showed that the main pore in AHTSS was a micropore with a mean pore size of 1.3 nm (analyzed by the DFT method, Fig. S7b†), further suggesting that AHTSS had abundant micropores, which were derived from closely stacked small TiO_2 NPs. It should be noted that micropores were unfavorable for AHTSS to disperse Pt NPs uniformly because they were unavailable to utilize the high SAA. In contrast, the SSA of UMTHS was reduced to $167.1 \text{ m}^2 \text{ g}^{-1}$ because of the formation of the urchin-like structure. In the inset of Fig. 1b, the dominant pore in UMTHS is a mesopore, which could be further verified from Fig. 2d and Fig. S5.† The mesopores in UMTHS originated from the bottom stacking among nanothorns.³⁰ Moreover, in Fig. 2e, it could be visually observed that the quantity of mesopores in UMTHS was significantly less compared to the quantity of micropores in AHTSS, and thus the SSA of UMTHS was less compared to that of AHTSS. Notably, the SSA of UMTHS was over three times higher than that of the commercial P25 ($50 \text{ m}^2 \text{ g}^{-1}$) and significantly surpassed the lowest SSA ($100 \text{ m}^2 \text{ g}^{-1}$) target set for the support.²⁵

3.2 Structure and morphology characterization of Pt/UMTHS and the reference Pt@C (w/o UMTHS) sample

Then, the UMTHS with a high SSA was successfully synthesized and applied as a support to disperse Pt NPs. Fig. 1a shows that the diffraction peaks of Pt with a face-centered cubic (fcc) structure appeared at the location of 39.4° , 45.5°

and 67.5° in Pt/UMTHS after annealing the mixture containing Pt-aniline and UMTHS at 600°C . These diffraction peaks corresponded to the (111), (200) and (220) planes of Pt, respectively. The XRD result illustrated that the Pt^{4+} cation was reduced to metallic Pt species after the heat treatment. Meanwhile, the UMTHS retained the anatase structure and showed a more sharp diffraction peak at 25.0° . For the reference Pt@C (w/o UMTHS) sample, except for the characteristic diffraction peaks of the Pt metal, a wide peak at the location of around 25° could be found (Fig. S8†), which could be assigned to the wide diffraction peak of amorphous carbon, because the XPS survey spectrum of the Pt@C (w/o UMTHS) sample revealed that only C (71.9%), Pt (7.7%), O (12.7%) and N (7.7%) elements existed in Pt@C (w/o UMTHS) (Fig. S9 and Table S2†). The XRD and XPS results of Pt@C (w/o UMTHS) illustrated that aniline would undergo polymerization and the product, polyaniline, would be carbonized and generate amorphous carbon and N species at 600°C .

TEM and HR-TEM were employed to check the morphology of Pt NPs. Sphere-like Pt NPs, which are mainly anchored on the rough surface of nanothorns in UMTHS, can be observed clearly in Fig. 2g and h. Besides, some UMTHS/carbon composites can also be seen in Fig. 2g. By magnifying the white solid square area inserted in Fig. 2h, clear and regular lattice fringes are observed in Fig. 2i with an interplanar distance of 0.226 nm, which corresponds to the (111) plane of fcc-Pt. Furthermore, the average size of Pt NPs is around 3.2 nm acquired by counting the size of 100 Pt NPs arbitrarily as shown in Fig. 2g. Such ultrafine Pt NPs can provide a higher mass activity for the ORR according to the result reported by Chorkendorff *et al.*³⁴ To explore whether the morphology of UMTHS would change a lot during the heat treatment at 600°C , SEM characterization was applied after Pt/UMTHS was obtained. From the SEM result in Fig. S10,† even though the UMTHS were heated to 600°C , most of them still retained the urchin-like sphere morphology with mild aggregation. Moreover, the BET result showed that Pt/UMTHS still exhibited a type-IV isotherm plot with a H3 hysteresis loop (Fig. S11†). The SSA of Pt/UMTHS increased to $262.7 \text{ m}^2 \text{ g}^{-1}$, probably because more mesopores and micropores were produced by the pyrolysis of polyaniline. However, in Fig. S11c,† it is clearly observed that slight aggregation occurs among Pt NPs in the Pt@C (w/o UMTHS) sample, although the mean particle size of Pt NPs (around 3.1 nm) is nearly identical to that of Pt/UMTHS (Fig. S12a and S12b†). Besides, as shown in Fig. S12d,† uneven carbon layers are formed with a thickness varying from 0.4 to 5 nm, which leads to less Pt surface exposed and is harmful for the effective diffusion of oxygen and the electrolyte. The results presented above demonstrated that using UMTHS with a high SSA as supports can disperse Pt NPs uniformly on their surface and can prevent the formation of a thick carbon layer.

As identified by an energy dispersive X-ray spectrometer, Ti, Pt and N elements were uniformly dispersed in Pt/UMTHS (Fig. S13†). The survey spectrum of Pt/UMTHS obtained from XPS also unveiled that the emission peaks of Ti, O, C, N and Pt

were located at their corresponding binding energy positions (Fig. S22a†). The high resolution spectrum of N 1s in Fig. S22c† could be resolved to pyridinic (398.3 eV), pyrrolic (400.3 eV), quaternary (401.1 eV), and oxidized N (403.0 eV) species.³⁵ Besides, pyrrolic N species were dominant in the N 1s high resolution XPS, which was consistent with the result that N tended to generate pyrrolic N species between 600 °C and 700 °C.³⁶ The Raman result also showed that there were four characteristic vibration peaks of anatase TiO₂ (E_g, B_{1g}, A_{1g} and E_g) and two peaks of carbon (D and G bands) in Pt/UMTHS (Fig. S14†).^{37,38} In order to check the accurate Pt content, the ICP-OES method was applied and the result showed that the Pt content of the Pt/UMTHS and Pt@C (w/o UMTHS) sample was 25.2% and 31.1%, respectively.

3.3 Activity and stability

The ORR activity of UMTHS, Pt/UMTHS and Pt@C (w/o UMTHS) was evaluated through CV and LSV curves. The as-synthesized Pt/UMTHS (without the addition of acetylene carbon black) exhibited a high ORR activity with a half-wave

potential of 0.83 V due to the formation of a UMTHS/carbon composite (Fig. S15†). As shown in Fig. 3a, it was obvious that Pt/UMTHS exhibited an excellent ORR activity while UMTHS exhibited no ORR activity, elucidating that ORR active sites originated from Pt NPs. The LSV curves of Pt/UMTHS obtained at different rotation rates (2500, 2000, 1600, 1200, and 900 rpm) are shown in Fig. S16.† The electron transfer number of Pt/UMTHS was obtained based on the RDE result through the Koutecky–Levich equation at 0.60–0.75 V. As shown in Fig. 3b, the electron transfer number of Pt/UMTHS was 3.86–3.94, revealing that the oxygen reduction mechanism of Pt/UMTHS was a four electron process.³⁹ Furthermore, Pt/UMTHS exhibited an extremely higher E_h than the reference sample Pt@C (w/o UMTHS) (0.867 V and 0.829 V, respectively), further indicating that the UMTHS support with a high SSA could disperse the Pt–aniline precursor well and prevent the formation of thick carbon layers. Even though little acetylene carbon black was added to Pt/UMTHS to further improve the conductivity of Pt/UMTHS, the improved conductivity is still inadequate, resulting in a slightly lower E_h in comparison to that of the

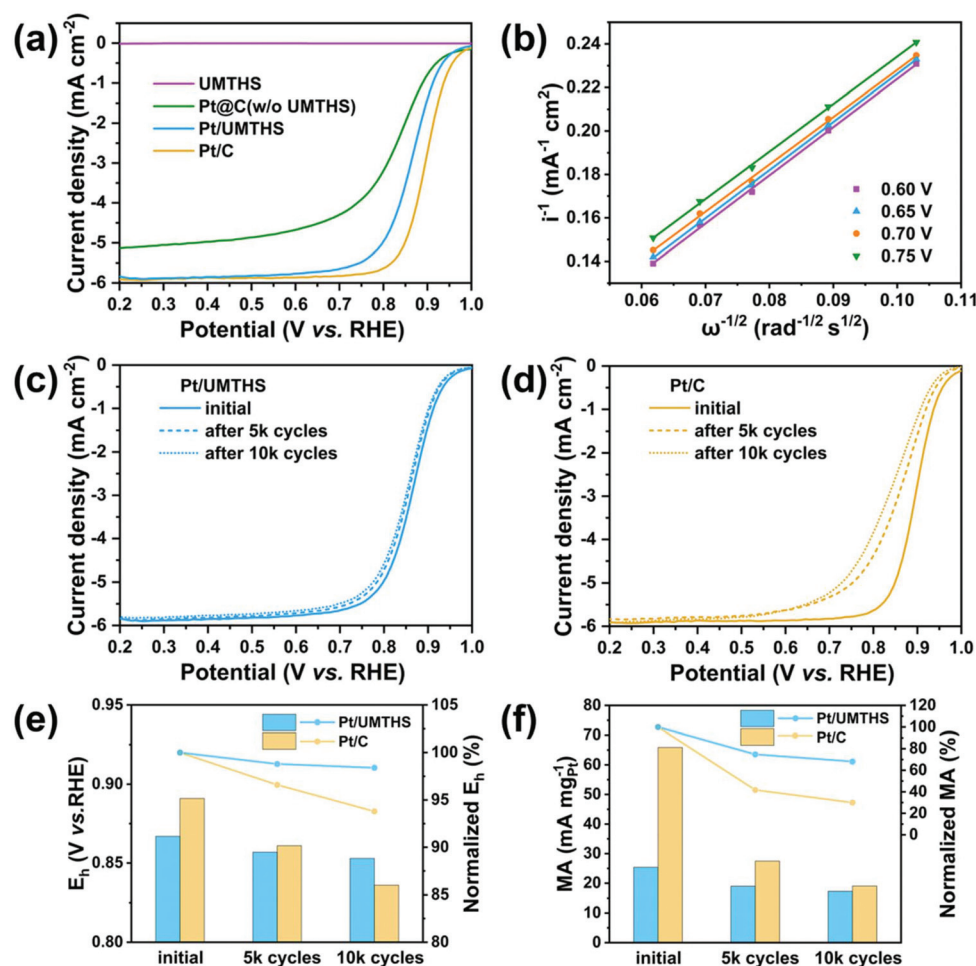


Fig. 3 (a) LSV curves of Pt/UMTHS, Pt/C, Pt@C (w/o UMTHS) and UMTHS in O₂-saturated 0.1 M HClO₄ at 1600 rpm (10 mV s⁻¹, 25 °C). (b) Koutecky–Levich plots obtained for Pt/UMTHS at 0.60–0.75 V. LSV curves of Pt/UMTHS (c) and the commercial Pt/C (d) obtained before and after different potential cycles in O₂-saturated 0.1 M HClO₄ at 0.6–1.0 V (1600 rpm, 10 mV s⁻¹, 25 °C). (e) Comparison of E_h and normalized E_h obtained from Fig. 3c and d. (f) Comparison of MA and normalized MA obtained from Fig. 3c and d.

commercial 20 wt% Pt/C (0.891 V). However, both Pt/UMTHS and Pt/C showed an identical diffusion limited current density (5.84 mA cm^{-2}) at 0.20–0.55 V (vs. RHE).

The accelerated durability test (ADT) was applied to assess the ORR stability of Pt/UMTHS and Pt/C. The LSV curves obtained after different potential cycles at 0.6–1.0 V for Pt/UMTHS and Pt/C are shown in Fig. 3c and d, respectively. As shown in Fig. 3c, it was obviously observed that the LSV curve of Pt/UMTHS exclusively showed a slight shift towards the left direction with a 1.6% loss of E_h after 10k potential cycles at 0.6–1.0 V. However, as shown in Fig. 3d, a much higher loss of E_h occurred in the commercial Pt/C (6.2%). The decrease of E_h for Pt/C was about 4 times higher than that of Pt/UMTHS. Moreover, Pt/UMTHS essentially retained its ECSA ($42.9 \text{ m}^2 \text{ g}_{\text{Pt}}^{-1}$) with a slight enhancement (2%) after 5k potential cycles (Fig. S17a and S17c†), probably because gentle carbon oxidation occurred on the surface of Pt NPs during the ADT and resulted in a little larger surface area of Pt NPs exposed. In contrast, in Fig. S17b,† obviously, the hydrogen absorption area of Pt/C at 0.11–0.44 V (vs. RHE) decreased gradually with a 7% loss of the ECSA after 10k potential cycles ($64.3 \text{ m}^2 \text{ g}_{\text{Pt}}^{-1}$ vs. $59.7 \text{ m}^2 \text{ g}_{\text{Pt}}^{-1}$, respectively, Fig. S17c†). More importantly, the MA of the Pt/C dropped drastically from $65.9 \text{ mA mg}_{\text{Pt}}^{-2}$ to $19.1 \text{ mA mg}_{\text{Pt}}^{-2}$ with an enormous loss of 71% after 10k potential cycles, which was nearly 2.2 times less in comparison to that of Pt/UMTHS (Fig. 3f). It is worth mentioning that the obtained MA for Pt/UMTHS ($17.3 \text{ mA mg}_{\text{Pt}}^{-2}$) after 10k potential cycles was comparable to that of Pt/C. The results presented above illustrated that Pt/UMTHS exhibited better stability than the commercial Pt/C during 10k potential cycles at 0.6–1.0 V and eventually exhibited a comparable ORR activity. In order to explore whether there are changes occurring in the morphology of Pt NPs after the ADT at 0.6–1.0 V, the catalyst thin films were collected by sonication and centrifugation and then studied by HR-TEM. As shown in Fig. 4a–d and S18,† the size of Pt NPs in Pt/UMTHS grew from 3.2 to 4.1 nm with 28% increase after 10k potential cycles, and retained their mor-

phology with no aggregation. However, significant aggregation could be seen in the commercial Pt/C, the Pt NPs grew from 2.5 to 5.3 nm with 112% increase (Fig. 4g, h, S19a and S19b†), indicating that the dissolution and/or aggregation of Pt NPs in Pt/UMTHS have been mitigated a lot as compared to that of Pt/C. Besides, Pt/UMTHS exhibited a better ORR stability than the samples reported in recent five years. As shown in Fig. S20,† it could be found that Pt/UMTHS showed less loss in both E_h and ECSA after the ADT as compared to the results of other TiO_2 -supported Pt-based ORR catalysts published by several literature studies.^{17,40–45} The corresponding data were compared and are listed in Table S1.† Carbon was present in Pt/UMTHS for the improvement of conductivity. To check whether the ORR performance of Pt/UMTHS will be affected by carbon corrosion, the accelerated durability test at 1.0–1.4 V for Pt/UMTHS was investigated. As shown in Fig. S21a,† Pt/UMTHS nearly retained its ORR activity with a slight decrease ($\sim 5 \text{ mV}$) of E_h after 8k potential cycles while the E_h of Pt/C decreased by about 40 mV (Fig. S21b†), which suggested that carbon corrosion had less influence on the ORR performance of the Pt/UMTHS than that of the Pt/C.

3.4 Enhanced stability mechanism of Pt/UMTHS

The enhanced stability of Pt/UMTHS needed to be clarified. XPS characterization was then applied to investigate the chemical states and binding environment of all elements for UMTHS and Pt/UMTHS samples. For comparison, the binding energies of all elements presented in their high resolution XPS spectrum have been calibrated according to the charge referenced to the C–C peak at 284.8 eV (Fig. S22b†).⁴⁶ In the UMTHS sample, the high resolution XPS of Ti 2p showed two bands at the positions of 464.6 eV and 458.8 eV, which were assigned to the emission peak of $2p_{1/2}$ and $2p_{3/2}$ of Ti^{4+} , respectively (Fig. 5a).⁴³ After integrating with Pt NPs, these two peaks shifted towards higher binding energy with an increment of 0.4 eV and 0.5 eV, respectively, indicating that the electronic property of Ti atoms changed to more positive.^{14,22,44}

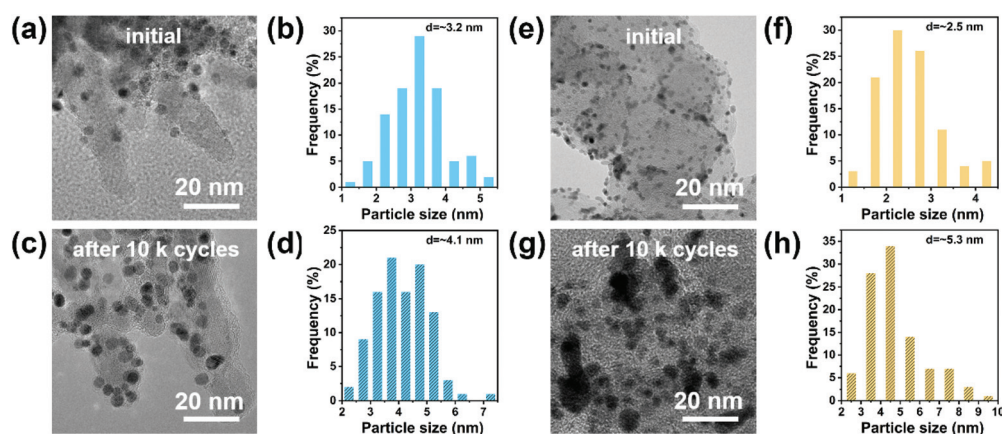


Fig. 4 *Ex situ* HR-TEM images of Pt/UMTHS obtained before (a) and after 10k potential cycles (c), and their size distribution of Pt NPs before (b) and after 10k potential cycles (d). *Ex situ* HR-TEM images of Pt/C obtained before (e) and after 10k potential cycles (g), and the size distribution of Pt NPs before (f) and after 10k potential cycles (h).

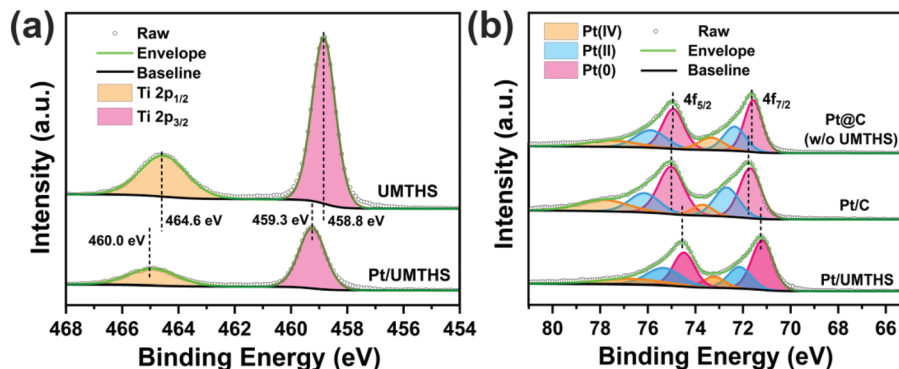


Fig. 5 (a) High resolution Ti 2p XPS spectrum of UMTHS and Pt/UMTHS. (b) High resolution Pt 4f XPS spectrum of Pt@C (w/o UMTHS), Pt/C and Pt/UMTHS.

Moreover, the Pt 4f XPS spectrum is shown in Fig. 5b. The Pt 4f_{7/2} and Pt 4f_{5/2} emission peak of Pt/UMTHS could be resolved into three peaks separately. Each of them belonged to Pt metal (71.3 and 74.6 eV), Pt²⁺ (72.2 and 75.2 eV) and Pt⁴⁺ (74.4 and 78.0 eV) species, respectively.⁴⁷ For comparison, the commercial Pt/C was also analyzed by XPS. As shown in Fig. 5b, a decrease of 0.5 eV could be found in the positions of both Pt 4f_{7/2} and Pt 4f_{5/2} emission peaks in Pt/UMTHS as compared to those of Pt/C, which elucidated that the electronic property of Pt atoms changed to more negative in Pt/UMTHS.^{12,19,23} Besides, a higher binding energy shift of O 1s could be found in Pt/UMTHS. As shown in Fig. S22d,† there were a dominant peak (530.1 eV) and a broader peak (531.4 eV) of O 1s for UMTHS, corresponding to Ti–O and Ti–OH bonds, respectively.^{43,47} In contrast, the position of these two O 1s emission peaks in Pt/UMTHS moved to 530.5 and 532.5 eV, increasing by 0.4 eV and 1.1 eV, respectively. Based on the above XPS results, it could be concluded that a SMSI exists between UMTHS and Pt NPs in Pt/UMTHS.

To explore the interaction between N species and Pt NPs in Pt/UMTHS, the position shifts of Pt 4f emission peaks were also checked for Pt@C (w/o UMTHS). As shown in Fig. 5b, compared with the positions of both Pt 4f_{7/2} and Pt 4f_{5/2} emission peaks of Pt/C, a slight decrease (<0.2 eV) could be found in those of Pt@C (w/o UMTHS), suggesting very weak interaction between Pt NPs and carbon support in Pt@C (w/o UMTHS). In contrast, the SMSI between UMTHS and Pt NPs played an important role in the decrease of the positions of Pt 4f emission peaks in Pt/UMTHS. Thus, the interactions between the carbon/N-carbon support and Pt NPs in both Pt/C and Pt@C (w/o UMTHS) were weak. On combining the ADT results at 0.6–1.0 V, it can be concluded that the enhanced stability of Pt NPs can be attributed to SMSI.^{16–19} Furthermore, the unique urchin-like structure of UMTHS can supply Pt NPs with a spatial restriction effect, which can contribute to the enhanced stability of Pt/UMTHS. The spatial restriction originates from the uniform dispersion of Pt NPs and longer distance among Pt NPs due to the high SSA of UMTHS rather than the mesopores. As verified by the TEM and BET results of Pt/UMTHS (Fig. 2h and 1b), the anchoring position of Pt NPs

was on the surface of the nanothorns with a large specific surface area in UMTHS rather than in the mesopores, suggesting that the mesopores in UMTHS cannot play an important role in enhancing the stability of Pt NPs. The anti-resistance of TiO₂ also contributes to the enhanced stability, especially at high potential. Therefore, the enhanced stability of Pt/UMTHS was mainly ascribed to SMSI which can mitigate the dissolution, detachment and aggregation of Pt NPs during the accelerated durability test at 0.6–1.0 V and 1.0–1.4 V.

4. Conclusion

UMTHS with a high SSA (167.1 m² g^{−1}) were successfully synthesized by the hydrothermal method and used as a support for catalysts. The conductivity of Pt/UMTHS was improved and uniform Pt NPs (~3.2 nm) on the surface of nanothorns were obtained *via* annealing the mixture containing UMTHS and Pt–aniline complex. It was demonstrated that Pt/UMTHS exhibited better stability in the ORR than the commercial Pt/C, which was mainly due to SMSI between Pt NPs and UMTHS. Besides, as verified by the TEM, BET and ADT results, spatial restriction provided by UMTHS and the anti-restriction of UMTHS also contribute to the enhanced stability. UMTHS are exceedingly good potential alternatives for carbon black supports due to their corrosion resistance, high SSA and SMSI with Pt NPs.

Conflicts of interest

There are no conflicts to declare.

Acknowledgements

This research was supported by the National Natural Science Foundation of China (Grant No. U1732155 and 61721005), the NSF for Distinguished Young Scholars of Fujian Province (Grant No. 2017J07004), and the STS project of Fujian Province (Grant No. 2018T3004).

References

- 1 M. K. Debe, *Nature*, 2012, **486**, 43–51.
- 2 H. A. Gasteiger and N. M. Marković, *Science*, 2009, **324**, 48–49.
- 3 T. Suzuki, in *Polymer Electrolyte Fuel Cells 16*, 2016, vol. 75, pp. 423–434.
- 4 N. Cheng, L. Zhang, H. Jiang, Y. Zhou, S. Yu, L. Chen, H. Jiang and C. Li, *Nanoscale*, 2019, **11**, 16945–16953.
- 5 Y. Nie, L. Li and Z. Wei, *Chem. Soc. Rev.*, 2015, **44**, 2168–2201.
- 6 M. Shao, Q. Chang, J.-P. Dodelet and R. Chenitz, *Chem. Rev.*, 2016, **116**, 3594–3657.
- 7 C. Galeano, J. C. Meier, V. Peinecke, H. Bongard, I. Katsounaros, A. A. Topalov, A. Lu, K. J. J. Mayrhofer and F. Schueth, *J. Am. Chem. Soc.*, 2012, **134**, 20457–20465.
- 8 N. Cheng, M. N. Banis, J. Liu, A. Riese, X. Li, R. Li, S. Ye, S. Knights and X. Sun, *Adv. Mater.*, 2015, **27**, 277–281.
- 9 Y. Shao-Horn, W. C. Sheng, S. Chen, P. J. Ferreira, E. F. Holby and D. Morgan, *Top. Catal.*, 2007, **46**, 285–305.
- 10 X. X. Wang, V. Prabhakaran, Y. He, Y. Shao and G. Wu, *Adv. Mater.*, 2019, **31**, 1805126.
- 11 S.-Y. Huang, P. Ganesan, S. Park and B. N. Popov, *J. Am. Chem. Soc.*, 2009, **131**, 13898–13899.
- 12 J.-H. Kim, S. Chang and Y.-T. Kim, *Appl. Catal., B*, 2014, **158**, 112–118.
- 13 P. Dhanasekaran, S. V. Selvaganesh and S. D. Bhat, *J. Power Sources*, 2016, **304**, 360–372.
- 14 Y. Chang, C. Yuan, Y. Li, C. Liu, T. Wu, B. Zeng, Y. Xu and L. Dai, *J. Mater. Chem. A*, 2017, **5**, 1672–1678.
- 15 Z.-Z. Jiang, D.-M. Gu, Z.-B. Wang, W.-L. Qu, G.-P. Yin and K.-J. Qian, *J. Power Sources*, 2011, **196**, 8207–8215.
- 16 N. G. Akalework, C.-J. Pan, W.-N. Su, J. Rick, M.-C. Tsai, J.-F. Lee, J.-M. Lin, L.-D. Tsai and B.-J. Hwang, *J. Mater. Chem.*, 2012, **22**, 20977–20985.
- 17 Y. Jeon, Y. Ji, Y. I. Cho, C. Lee, D.-H. Park and Y.-G. Shul, *ACS Nano*, 2018, **12**, 6819–6829.
- 18 B. Y. Xia, B. Wang, H. B. Wu, Z. Liu, X. Wang and X. W. Lou, *J. Mater. Chem.*, 2012, **22**, 16499–16505.
- 19 J.-H. Kim, G. Kwon, H. Lim, C. Zhu, H. You and Y.-T. Kim, *J. Power Sources*, 2016, **320**, 188–195.
- 20 X. Liu, J. Chen, G. Liu, L. Zhang, H. Zhang and B. Yi, *J. Power Sources*, 2010, **195**, 4098–4103.
- 21 H. Van Thi Thanh, C.-J. Pan, J. Rick, W.-N. Su and B.-J. Hwang, *J. Am. Chem. Soc.*, 2011, **133**, 11716–11724.
- 22 R. A. M. Esfahani, I. I. Ebraliidze, S. Specchia and E. B. Easton, *J. Mater. Chem. A*, 2018, **6**, 14805–14815.
- 23 M. Eckardt, C. Gebauer, Z. Jusys, M. Wassner, N. Huesing and R. J. Behm, *J. Power Sources*, 2018, **400**, 580–591.
- 24 M. Carmo, A. R. Dos Santos, J. G. R. Poco and M. Linardi, *J. Power Sources*, 2007, **173**, 860–866.
- 25 Z. Sun, J. H. Kim, Y. Zhao, F. Bijarbooneh, V. Malgras, Y. Lee, Y.-M. Kang and S. X. Dou, *J. Am. Chem. Soc.*, 2011, **133**, 19314–19317.
- 26 Y. Holade, C. Morais, K. Servat, T. W. Napporn and K. B. Kokoh, *Phys. Chem. Chem. Phys.*, 2014, **16**, 25609–25620.
- 27 Y. Takasu, T. Kawaguchi, W. Sugimoto and Y. Murakami, *Electrochim. Acta*, 2003, **48**, 3861–3868.
- 28 X. Tang, Y. Zeng, L. Cao, L. Yang, Z. Wang, D. Fang, Y. Gao, Z. Shao and B. Yi, *J. Mater. Chem. A*, 2018, **6**, 15074–15082.
- 29 Y.-J. Wang, D. P. Wilkinson and J. Zhang, *Chem. Rev.*, 2011, **111**, 7625–7651.
- 30 J. H. Pan, X. Z. Wang, Q. Huang, C. Shen, Z. Y. Koh, Q. Wang, A. Engel and D. W. Bahnemann, *Adv. Funct. Mater.*, 2014, **24**, 95–104.
- 31 M. Karuppannan, Y. Kim, S. Gok, E. Lee, J. Y. Hwang, J.-H. Jang, Y.-H. Cho, T. Lim, Y.-E. Sung and O. J. Kwon, *Energy Environ. Sci.*, 2019, **12**, 2820–2829.
- 32 W. Gao, Z. Zhang, M. Dou and F. Wang, *ACS Catal.*, 2019, **9**, 3278–3288.
- 33 D. Wang, H. L. Xin, R. Hovden, H. Wang, Y. Yu, D. A. Muller, F. J. DiSalvo and H. D. Abruna, *Nat. Mater.*, 2013, **12**, 81–87.
- 34 F. J. Perez-Alonso, D. N. McCarthy, A. Nierhoff, P. Hernandez-Fernandez, C. Streb, I. E. L. Stephens, J. H. Nielsen and I. Chorkendorff, *Angew. Chem.*, 2012, **124**, 4719–4721.
- 35 J.-J. Cai, Q.-Y. Zhou, B. Liu, X.-F. Gong, Y.-L. Zhang, K. Goh, D.-M. Gu, L. Zhao, X.-L. Sui and Z.-B. Wang, *Nanoscale*, 2020, **12**, 973–982.
- 36 J. R. Pels, F. Kapteijn, J. A. Moulijn, Q. Zhu and K. M. Thomas, *Carbon*, 1995, **33**, 1641–1653.
- 37 R. Boppella, P. Basak and S. V. Manorama, *ACS Appl. Mater. Interfaces*, 2012, **4**, 1239–1246.
- 38 L. Zhao, X.-L. Sui, Q.-Y. Zhou, J.-Z. Li, J.-J. Zhang, G.-S. Huang and Z.-B. Wang, *J. Mater. Chem. A*, 2018, **6**, 6212–6219.
- 39 L. Zhao, X.-L. Sui, J.-Z. Li, J.-J. Zhang, L.-M. Zhang, G.-S. Huang and Z.-B. Wang, *Appl. Catal., B*, 2018, **231**, 224–233.
- 40 Y. Ji, Y. I. Cho, Y. Jeon, C. Lee, D.-H. Park and Y.-G. Shul, *Appl. Catal., B*, 2017, **204**, 421–429.
- 41 M. Kim, C. Kwon, K. Eom, J. Kim and E. Cho, *Sci. Rep.*, 2017, **7**, 44411.
- 42 M.-C. Tsai, N. Trung-Thanh, N. G. Akalework, C.-J. Pan, J. Rick, Y.-F. Liao, W.-N. Su and B.-J. Hwang, *ACS Catal.*, 2016, **6**, 6551–6559.
- 43 P. S. M. Kumar, V. K. Ponnusamy, K. R. Deepthi, G. Kumar, A. Pugazhendhi, H. Abe, S. Thiripuranthagan, U. Pal and S. K. Krishnan, *J. Mater. Chem. A*, 2018, **6**, 23435–23444.
- 44 C. H. Sung, R. Boppella, J.-W. Yoo, D.-H. Lim, B.-M. Moon, D. H. Kim and J. Y. Kim, *Adv. Mater. Interfaces*, 2017, **4**, 1700564.
- 45 P. Dhanasekaran, S. V. Selvaganesh, A. Shukla, N. Nagaraju and S. D. Bhat, *Electrochim. Acta*, 2018, **263**, 596–609.
- 46 C. Hu, Y. Xiao, Y. Zhao, N. Chen, Z. Zhang, M. Cao and L. Qu, *Nanoscale*, 2013, **5**, 2726–2733.
- 47 J. Wang, M. Xu, J. Zhao, H. Fang, Q. Huang, W. Xiao, T. Li and D. Wang, *Appl. Catal., B*, 2018, **237**, 228–236.